Microstructured layered-kagome BaCo 3 (VO 4) 2 (OH) 2 with variable crystallite size: alternative synthetic route and comparison with nanostructured samples

Bachchar Hadrane, Philippe Deniard, Cassandre Jeannot, Isabelle Trenque, Rémi Dessapt, Christophe Payen

ARTICLE

Microstructured layered-kagome $BaCo_3(VO_4)_2(OH)_2$ with variable crystallite size: alternative synthetic route and comparison with nanostructured samples

Received 00th January 20xx,
Accepted 00th January 20xx

DOI: 10.1039/x0xx00000x

Bachchar Hadrane[a], Philippe Deniard[a], Cassandre Jeannot[a], Isabelle Trenque[a], Rémi Dessapt*[a] and Christophe Payen*[a]

Microplatelets of the layered-kagome compound $BaCo_3(VO_4)_2(OH)_2$, which is the Co^{2+} analogue of mineral vesignieite $BaCu_3(VO_4)_2(OH)_2$, have been prepared with very high yield by hydrothermal reaction using synthetic karpenkoite $Co_3V_2O_7(OH)_2.2H_2O$ as starting reagent. The Rietveld refinement of X-ray diffraction data indicates that $Co_3V_2O_7(OH)_2{\cdot}2H_2O$ is isostructural with martyite $Zn_3V_2O_7(OH)_2{\cdot}2H_2O$. Two single-phased samples of microstructured $BaCo_3(VO_4)_2(OH)_2$ have been characterized using powder X-ray diffraction, FT-IR and Raman spectroscopies, thermal analyses, scanning electron microscopy, energy-dispersive X-ray spectroscopy and magnetisation measurements. Their crystallite sizes perpendicular to the *c*-axis are in the range of 92(3) to 146(6) nm and depend on the synthesis conditions. Results have been compared to those previously obtained for quasi-spherical nanoparticles having a crystallite size of the order of 20 nm, to explore the effect of the crystallite size on the properties of $BaCo_3(VO_4)_2(OH)_2$. This study highlights that the magnetic properties depend on the crystallite sizes only at low temperatures.

Introduction

The family of divalent transition-metal orthovanadates $BaM_3(VO_4)_2(OH)_2$ where M = Co, Ni, Cu has received a good deal of attention in the last two decades, essentially because their crystal structures comprise kagome arrays of magnetic ions.[1–14] Kagome compounds are of great interest due to their complex and unusual magnetic behaviour resulting from geometric frustration.[15,16] All three $BaM_3(VO_4)_2(OH)_2$ compounds have similar crystal structures which are built up of $M_3O_6(OH)_2$ brucite-like layers.[17,12,18] These layers are formed from edge-sharing $MO_4(OH)_2$ octahedra and are kept apart by VO_4 vanadate groups and Ba^{2+} ions. Fig. 1 gives a schematic representation of the structure of the Co-based member $BaCo_3(VO_4)_2(OH)_2$.[18] The most studied compound is the synthetic analogue of copper mineral vesignieite $BaCu_3(VO_4)_2(OH)_2$, which is a well-known spin-1/2 kagome antiferromagnet with a Weiss temperature $\theta \approx -80$ K.[1–11] This compound orders magnetically at $T_N = 9$ K, and a dynamic Jahn-Teller effect persists below T_N indicating concomitant spin and orbital frustration. The less-studied spin-1 nickel member $BaNi_3(VO_4)_2(OH)_2$ exhibits a glassy magnetic transition at low temperature.[12] $BaCo_3(VO_4)_2(OH)_2$, which is the focus of this work, was first obtained with moderate yield by hydrothermal reaction, from a mixture of $Ba(OH)_2{\cdot}H_2O$, Co powder and V_2O_5.[18] Its crystal structure was solved to be a rhombohedral $R\bar{3}m$ system with regular kagome planes of edge-sharing $CoO_4(OH)_2$ octahedra. However, only very small single-crystals were obtained together with impurities, thus hindering further investigations of their physical properties. Recently, we reported a new soft-chemistry route to quantitatively obtain pure quasi-spherical and highly crystalline nanoparticles (NPs) of $BaCo_3(VO_4)_2(OH)_2$ with size in the range of 9-25 nm, by a coprecipitation method at ambient pressure.[13] We have demonstrated that nanostructuring does not affect the crystal structure even at the atomic scale. Magnetic susceptibility data at high temperature (T > 150 K) are consistent with high-spin d^7 Co^{2+} ions in octahedral environment. This compound was therefore identified as a candidate in the search for new quantum magnets with spin-orbit coupling.[13] No superparamagnetic blocking temperature or spin-glass transition were detected above 2 K, yet the magnetic behaviour could be affected by finite-size or surface effects at low temperature. Very recently, Y. Haraguchi et al. reported the magnetic properties of polycrystalline samples produced via a hydrothermal route that used $Ba(OH)_2.8H_2O$, $CoCl_2.2H_2O$, and NH_4VO_3 as reagents.[14] Magnetic measurements suggested that bulk $BaCo_3(VO_4)_2(OH)_2$ possesses a canted antiferromagnetic order below 2.7 K and behaves as an effective spin J_{eff} = ½ magnet at low temperatures. Analysis of powder X-ray diffraction (XRD) data was performed using the published structural model in ref.[18] without refining any structural parameters or determining crystallite sizes.

[a] Nantes Université, CNRS, Institut des Matériaux de Nantes Jean Rouxel, IMN, F-44000 Nantes, France
* Email: remi.dessapt@cnrs-imn.fr, christophe.payen@cnrs-imn.fr

Electronic Supplementary Information (ESI) available: Rietveld refinement plot, structural parameters, crystal structure and SEM image of $Co_3V_2O_7(OH)_2{\cdot}2H_2O$, EDS spectrum for **$BaCo_3$-A**, TG curve for **$BaCo_3$-B**, Rietveld refinement plot for **$BaCo_3$-B**, structural parameters for **$BaCo_3$-B**, FT-IR and Raman spectra for **$BaCo_3$-B**, magnetic field dependence of magnetisation for **$BaCo_3$-B**, fragment of a kagome layer in $BaCo_3(VO_4)_2(OH)_2$. See DOI: 10.1039/x0xx00000x

In this paper, we report an alternative synthetic strategy to obtain microstructured $BaCo_3(VO_4)_2(OH)_2$ via hydrothermal treatment of $Co_3V_2O_7(OH)_2{\cdot}2H_2O$, which is the synthetic analogue of mineral karpenkoite,[19] in $Ba(CH_3COO)_2$ aqueous solution. This synthetic route is inspired by previously published works that reported the preparation of vesignieite $BaCu_3(VO_4)_2(OH)_2$ by heating powders or crystals of volborthite $Cu_3V_2O_7(OH)_2{\cdot}2H_2O$ either at ambient pressure[20] or under hydrothermal conditions.[8,9] Two polycrystalline $BaCo_3(VO_4)_2(OH)_2$ samples, hereafter labelled as **$BaCo_3$-A** and **$BaCo_3$-B**, with crystallite sizes perpendicular to the *c*-axis of 146(6) and 92(3) nm, respectively, have been obtained by varying the cooling rate during the hydrothermal synthesis. The cooling rate also impacts the yield of synthesis. **$BaCo_3$-A** and **$BaCo_3$-B** have been fully characterized using XRD, thermal analyses, FT-IR and Raman spectroscopies, scanning electron microscopy (SEM), energy-dispersive X-ray spectroscopy (EDS), and magnetisation measurements. Results have been compared to those previously obtained for crystalline $BaCo_3(VO_4)_2(OH)_2$ NPs,[13] to discuss the impact of nanostructuring on the magnetic properties. We also provide for the first time refined structural parameters deduced from a Rietveld refinement of XRD data for $Co_3V_2O_7(OH)_2{\cdot}2H_2O$, which unambiguously indicates that it is isostructural with $Zn_3V_2O_7(OH)_2{\cdot}2H_2O$.

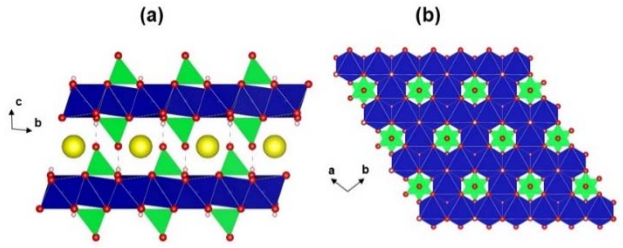

Fig. 1 Crystal structure of $BaCo_3(VO_4)_2(OH)_2$.[18] (a) Projection along the [100] direction. (b) View along the [001] direction showing a fragment of a kagome layer of edge-sharing $CoO_4(OH)_2$ octahedra. Blue octahedra: CoO_6, green tetrahedra: VO_4, red sphere: oxygen, yellow sphere: barium, white sphere: hydrogen. Hydrogen bonds are displayed as grey dashed lines.

Experimental

Synthesis

$Co_3V_2O_7(OH)_2{\cdot}2H_2O$ was first obtained as a microcrystalline powder by a hydrothermal method derived from a reported procedure.[21] Powder samples of $Co_3V_2O_7(OH)_2{\cdot}2H_2O$ were characterized by XRD and SEM as described below. **$BaCo_3$-A** and **$BaCo_3$-B** were then synthesized in a reproducible manner under mild hydrothermal conditions. $Co_3V_2O_7(OH)_2{\cdot}2H_2O$ (0.1 g; 2.17 10^{-1} mmol) was introduced into an aqueous solution (10 mL) of barium acetate $Ba(CH_3COO)_2$ (0.089 g; 3.48 10^{-1} mmol). The mixtures were stirred for a few minutes under moderate heating and sealed in 23 mL Teflon-lined autoclaves which were then heated from room temperature to 200 °C at a rate of 1 °C/min, and left for 24 hours in autogenous pressure conditions. The autoclave was cooled to room temperature at a rate of 15 °C/hour for **$BaCo_3$-A**, and of 60°C/hour for **$BaCo_3$-B**. After filtration, the obtained light-brown powders were washed with water and ethanol, and dried in air at room temperature. Yields are 94% and 68% for **$BaCo_3$-A** and **$BaCo_3$-B**, respectively.

Characterisation Methods

SEM images and EDS spectra were obtained with a JEOL JSM 7600F and JEOL JSM 5800LV scanning electron microscopes, respectively. EDS analyses were carried out on thin pellets. X-ray diffraction measurements were performed on a D8 Bruker diffractometer employing the CuK-L3 radiation (Ge (111) monochromator) and a Lynxeye 1D detector in the 5–110° 2θ interval, with 0.014° steps of 1.44s each. A total acquisition time of about 3 hours was necessary to obtain patterns with a good enough signal to noise ratio because of the fluorescence due to the cobalt-containing samples. Structure refinements were carried out with the Jana2020 software,[22] using the Rietveld procedure with the fundamental parameter approach.[23–25] This approach makes possible the deconvolution of the X-ray line profile diffractometer (X-ray energy dispersion and optics) and the specimen itself without the need for a standard. Nitrogen volumetric measurement treated by the Brunauer-Emmett-Teller (BET) approaches were recorded on a micrometrics ASAP 2010 device. Thermogravimetric analysis (TGA) were performed in flowing air at a heating rate of 5 °C min^{-1} on a SETARAM TG-DSC 111 between room temperature and 800 °C. FT-IR spectra were recorded at room temperature in the 4000-400 cm^{-1} range on a BRUKER Vertex. Room temperature Raman spectra were collected under microscope in backward scattering configuration using a Renishaw InVia spectrometer and the 633 nm line of an argon ion laser. The laser probe diameter at the sample surface was approximately 2 µm. The laser power was reduced to about 0.1 mW to avoid sample heating. Two edge filters were used to filter the Rayleigh line intensity, allowing measurements above 100 cm^{-1}. Spectra were recorded at 2 cm^{-1} resolutions over the wavenumber range -20-1900 cm^{-1}, with 4 scan accumulation (with 10 s as exposure time). SQUID magnetometers (Quantum Design, MPMS) were used to collect temperature and field dependent dc magnetization data. The susceptibility was defined as the ratio of the magnetization M to the small applied field H = 100 Oe, $\chi = M/H$.

Results and discussion

Synthesis and Physicochemical Characterizations

$BaCo_3(VO_4)_2(OH)_2$ powdered samples have been prepared by hydrothermal reaction of synthetic microcrystalline powders of karpenkoite $Co_3V_2O_7(OH)_2{\cdot}2H_2O$ in a $Ba(CH_3COO)_2$ aqueous solution. Noticeably, the cooling rate from 200°C to room temperature significantly impacts the yield of the synthesis which increases from 68% for **$BaCo_3$-B** to 94% for **$BaCo_3$-A**, by decreasing the cooling rate from 60 °C/hour to 15 °C/hour.
The cobalt pyrovanadate $Co_3V_2O_7(OH)_2{\cdot}2H_2O$ has been thought to be isostructural to the synthetic analogue of mineral martyite

$Zn_3V_2O_7(OH)_2{\cdot}2H_2O$, based on the comparison of X-ray diffraction patterns with JCPDS files no. 50-0570 or 87-0417 for $Zn_3V_2O_7(OH)_2{\cdot}2H_2O$.[21,26] To our knowledge, however, no refined structural parameters have been reported so far. This prompted us to perform a Rietveld refinement of the XRD pattern of $Co_3V_2O_7(OH)_2{\cdot}2H_2O$ using the published $P\bar{3}m$ structural model of $Zn_3V_2O_7(OH)_2{\cdot}2H_2O$.[27] The final Rietveld plot is shown in Fig. S1, ESI†. The refined structural parameters (Table S1, ESI†) are very close to those previously reported for $Zn_3V_2O_7(OH)_2{\cdot}2H_2O$, well demonstrating that both compounds are isostructural. As for $BaCo_3(VO_4)_2(OH)_2$, the structure of $Co_3V_2O_7(OH)_2{\cdot}2H_2O$ is built up of $Co_3O_6(OH)_2$ kagome layers. These layers are connected along the *c*-axis by pyrovanadates groups, and water molecules occupy large cavities between the layers (Fig. S2, ESI†). The refined crystallite sizes are in the range of 162-354 nm perpendicular to [001]. A SEM image of a representative microstructured sample of $Co_3V_2O_7(OH)_2{\cdot}2H_2O$ is given in Fig. S3, ESI†.

For $BaCo_3(VO_4)_2(OH)_2$, Ba/Co, Ba/V and Co/V elemental ratios were determined by EDS analyses (Fig. S4, ESI†) and were equal to 0.33, 0.50 and 1.48, for **$BaCo_3$-A** and to 0.37, 0.51 and 1.39, for **$BaCo_3$-B**. These values are in good agreement with the expected ones (0.33, 0.50 and 1.50, respectively). The TGA curve of **$BaCo_3$-B** shows one weight loss of 3.23% in the temperature range of 25−590 °C (Fig. S5, ESI†). This can be attributed to removal of one water molecule (theoretical weight loss of 3.11%), arising from the decomposition of the two hydroxyl groups.

The purity and crystallinity of the $BaCo_3(VO_4)_2(OH)_2$ samples were confirmed by XRD analyses at room temperature. Their structure was refined starting from the $R\bar{3}m$ structural model of ref..[18] Final refinement plots are shown in Fig. 2 and in Fig. S6, ESI† for **$BaCo_3$-A** and **$BaCo_3$-B**, respectively. Final reliability factors and refined structural parameters are given in Table 1 and Table S2, ESI† for **$BaCo_3$-A** and **$BaCo_3$-B**, respectively. For both samples, structural parameters are in good agreement with those previously obtained for single crystals.[18] The crystal structure displayed in Fig. 1 was carefully described and compared to related compounds in ref..[18] Compared to the isotropic crystallite size of $BaCo_3(VO_4)_2(OH)_2$ NPs which was evaluated to about 22 nm,[13] the micrometric $BaCo_3(VO_4)_2(OH)_2$ samples show much higher crystallite sizes of 146(6) and 92(3) nm in the (*ab*) plane for **$BaCo_3$-A** and **$BaCo_3$-B**, respectively. The crystallite sizes along the *c*-axis, 38(8) and 47(5) nm for **$BaCo_3$-A** and **$BaCo_3$-B**, respectively, are smaller than the in-plane ones and seem to be independent of the synthesis conditions.

The observed anisotropies of the crystallite size are consistent with the particle shapes as revealed by SEM. As can be seen in Fig. 3, the two samples consist of microplatelets with sizes in the approximate ranges of 0.5-10 and 0.1-5 µm for **$BaCo_3$-A** and **$BaCo_3$-B**, respectively. As expected from these SEM analyses, the microstructured powders exhibit a very low specific surface of about 2 $m^2\ g^{-1}$ which strongly contrasts with that of 61 $m^2\ g^{-1}$ previously obtained for $BaCo_3(VO_4)_2(OH)_2$ NPs.[13]

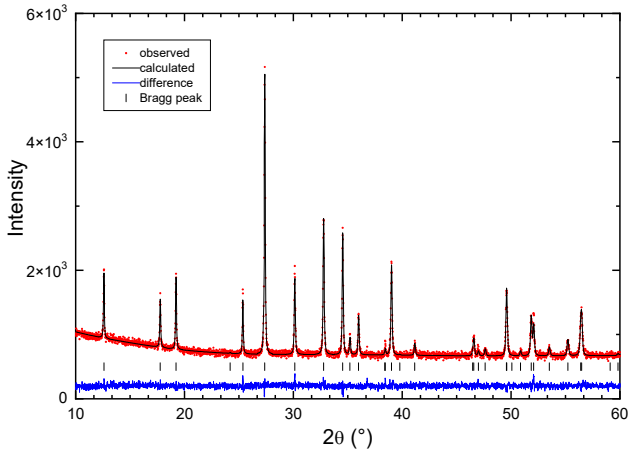

Fig. 2 Rietveld refinement plot for microstructured **$BaCo_3$-A** showing observed, calculated and difference patterns. The high-level noisy pattern is due to cobalt fluorescence.

Table 1 Structural parameters, final agreement factors and crystallite size for **$BaCo_3$-A.**

S.G. $R\bar{3}m$: a=5.92655(15) Å, c=21.0552(6) Å Cryst. size=146(6) nm ⊥ [001], 38(8) nm // [001]					
Atom	x	y	z	SOF	U_{iso} Equiv (Å²)
Ba_1	0.6667	0.3333	0.8333	1	0.036 (2)
Co_1	0.8333	0.6667	0.6667	1	0.025 (2)
V_1	0.3333	0.6667	0.7529 (2)	1	0.022 (3)
O_1	0.3333	0.6667	0.8327(7)	1	0.020 (3)
O_2	0.4983(10)	0.5017(10)	0.7285 (4)	1	0.020
O_3	0	0	0.7118(10)	1	0.020
H_1	0	0	0.7494*	1	0.008*
GOF= 1.14, Rwp= 4.12 and Rp= 3.24					

*not refined

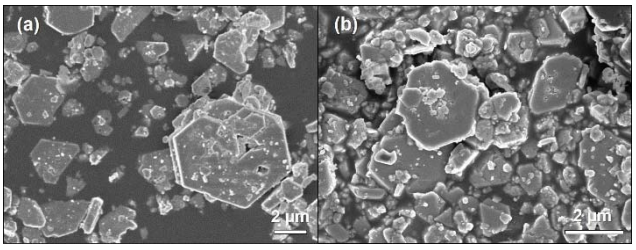

Fig. 3 SEM images of representative microstructured samples of (a) **$BaCo_3$-A** and (b) **$BaCo_3$-B**.

$BaCo_3$-A and **$BaCo_3$-B** were then characterized by FT-IR and Raman spectroscopies. Fig. 4 shows a comparison between the FT-IR and Raman spectra of **$BaCo_3$-A** and those previously reported for the $BaCo_3(VO_4)_2(OH)_2$ NPs.[13] In the range of 1000-400 cm^{-1}, the infrared vibration bands, which can be mainly attributed to V-O and Co-O stretching modes, are highly comparable for both micro- and nanostructured samples (Fig. 4(a)). Their Raman spectra also exhibit similar peaks in the range of 100–1100 cm^{-1} (Fig. 4(b)). However, microstructuring significantly impacts the profile of the Raman peaks which are much thinner for **$BaCo_3$-A** than for the NPs. Similar results have been obtained for **$BaCo_3$-B** (Fig. S7, ESI†).

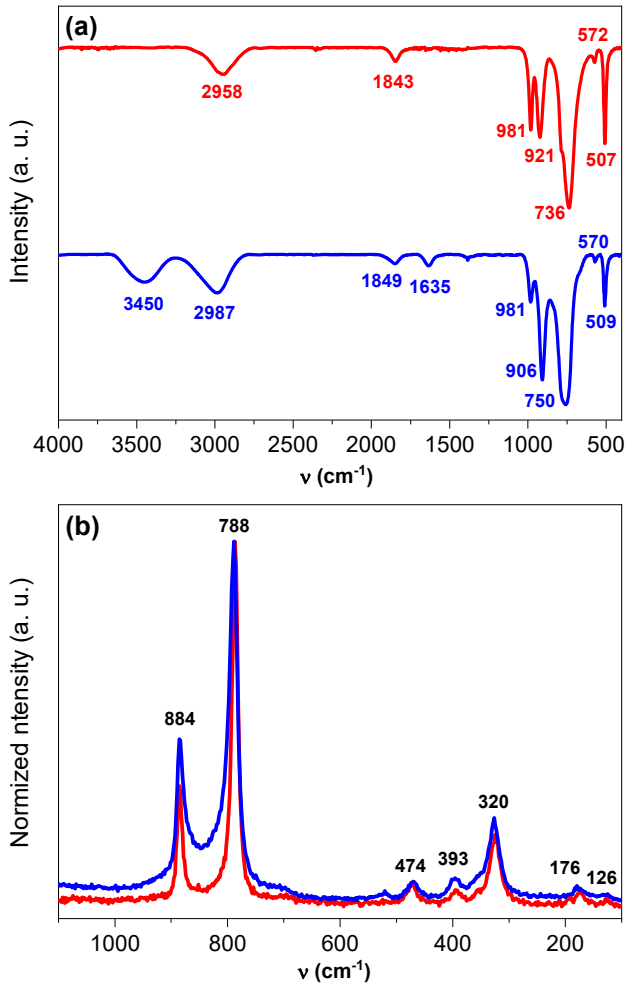

Fig. 4 Comparison of (a) FT-IR and (b) Raman spectra of microstructured **$BaCo_3$-A** (red line) and $BaCo_3(VO_4)_2(OH)_2$ nanoparticles[13] (blue line).

Magnetic Properties

Temperature dependences of the inverse magnetic susceptibilities, $1/\chi(T)$, of **$BaCo_3$-A** and **$BaCo_3$-B** are shown in Fig. 5. At high temperatures, susceptibilities follow a Curie-Weiss law $\chi = C/(T-\theta)$. Fits to this law between 150 K and 300 K yield the values C = 9.50(1) cm^3 K mol^{-1} and θ = - 26.6(3) K for **$BaCo_3$-A**, and C = 9.08(1) cm^3 K mol^{-1} and θ = - 29.7(3) K for **$BaCo_3$-B**. The fitted C values corresponds to effective magnetic moments μ_{eff} of ≈ 5.04 and ≈ 4.92 μ_B/Co-atom for **$BaCo_3$-A** and **$BaCo_3$-B** respectively. These μ_{eff} values are consistent with high-spin Co^{2+} ions in a weak octahedral crystal field. Experimental effective paramagnetic moments for octahedral high-spin Co^{2+} ions are larger than the spin-only value for S = 3/2 (3.87 μ_B) due to an unquenched orbital angular momentum.[28] The negative Weiss temperatures are slightly smaller than the values previously reported for a polycrystalline sample (-22.7(2) K)[14] and for NPs (-22.4(4) K).[13] Thus, it appears that the high-temperature magnetic susceptibility is not significantly affected by the crystallite size. This can be also seen from the $\chi(T).T$ product versus temperature T plot shown in Fig. 6. Both the $\chi(T).T$ values at 300 K and the smooth decreases in $\chi(T).T$ with decreasing temperature are consistent with theoretical expressions of the susceptibility of a six-coordinated high-spin Co^{2+} mononuclear complex.[28,29] Below ≈ 5 K, the $\chi(T).T$ products of the microstructured samples sharply increase, suggesting the onset of ferromagnetic correlations. There is a maximum in the $\chi(T).T$ data at 2.6 K (for **$BaCo_3$-A**) or 2.5 K (for **$BaCo_3$-B**), indicating a magnetic transition. As can be seen in Fig. 7, the low-temperature ZFC and FC susceptibilities of **$BaCo_3$-B** increase down to 2 K with a small difference between the ZFC and FC data below 2.5 K. For **$BaCo_3$-A**, which has the highest crystallite size in the (ab) plane, a maximum is observed in the ZFC trace at 2.4 K and a ZFC-FC bifurcation occurs below this temperature. These findings suggest that a weak ferromagnetic order sets in at low temperature (2-3 K) in the microstructured samples, consistent with recent results obtained for a polycrystalline sample with unknown crystallite sizes.[14]

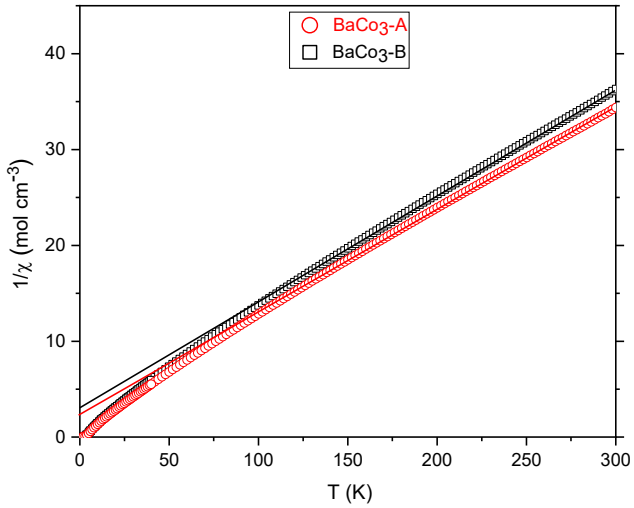

Fig. 5 Inverse magnetic susceptibility $1/\chi$ versus temperature *T* for **$BaCo_3$-A** and **$BaCo_3$-B,** as measured under zero-field-cooled conditions at 100 Oe. Solid lines denote the Curie-Weiss fits from 150 to 300 K.

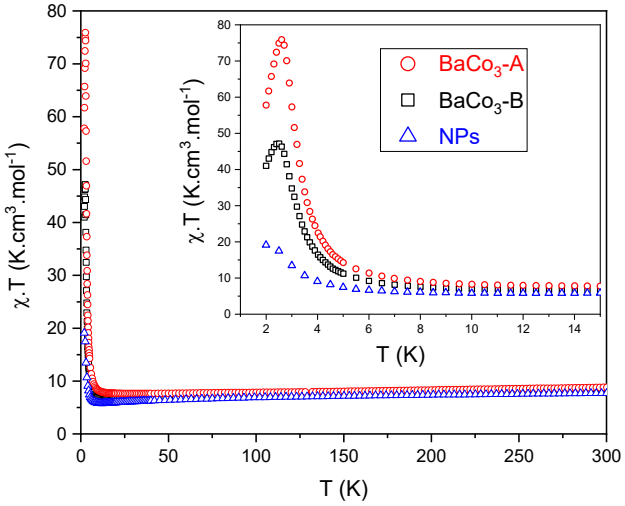

Fig. 6 Temperature dependence of the $\chi(T).T$ product for **$BaCo_3$-A**, **$BaCo_3$-B** and $BaCo_3(VO_4)_2(OH)_2$ nanoparticles[13] (NPs). Data were acquired under zero-field-cooled conditions at an applied magnetic field of 100 Oe. Insert: enlargement of $\chi(T).T$ below 15 K.

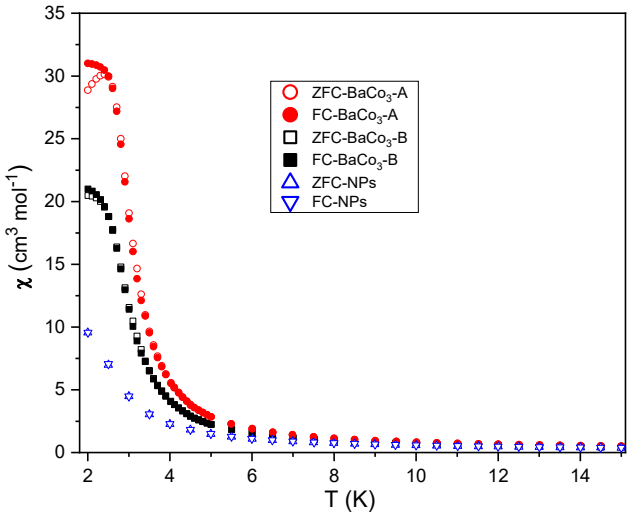

Fig. 7 Zero-field cooled (ZFC) and field cooled (FC) magnetic susceptibilities $\chi(T)$ at low temperatures, $T \leq 15$ K, for **$BaCo_3$-A**, **$BaCo_3$-B**, and $BaCo_3(VO_4)_2(OH)_2$ nanoparticles[13] (NPs). All data were acquired at an applied field of 100 Oe.

To investigate the magnetic properties further, we collected isothermal magnetisation data M(H) at several temperatures below 50 K for **$BaCo_3$-A** (Fig. 8) and **$BaCo_3$-B** (Fig. S8, ESI†). Very similar behaviours are observed for both microstructured samples. Similar trends were reported for the NPs.[13] At 50 K, the anticipated linear paramagnetic variation of M(H) is observed. The shape of the isothermal M(H) curve strongly changes when lowering the temperature to the range where the $\chi(T)$.T product rapidly increases. At T = 2 K, the isothermal curves of both microstructured samples have the form typical for an antiferromagnet with a weak ferromagnetic moment. As *H* increases, there is an immediate increase in *M*. Once the saturation of the weak ferromagnetic moment has been reached, M almost linearly increases to ≈ 25 000 emu/mol (1.4-1.5 μ_B/Co-atom) at 70 000 Oe.

These low-temperature behaviours can be explained by a weak ferromagnetism due to spin canting. As recently suggested, a Dzyaloshinsky-Moriya interaction may give each kagome layer a net ferromagnetic moment by canting the spins slightly out of the kagome plane.[14] It is also plausible that the single-ion anisotropy mechanism for spontaneous spin canting occurs because the kagome layers are formed from compressed $CoO_4(OH)_2$ octahedra that are tilted to each other (see Fig. S9, ESI†). The directions of the local easy axis on the Co^{2+} sites could therefore differ from each other. For high-spin Co^{2+} ions in a weak octahedral crystal field, the magnetic moments are expected to be anisotropic due to spin-orbit coupling.[30] For instance, an Ising anisotropy with *c* as the magnetic easy axis is observed for $BaCo_2V_2O_8$ (S.G. $I4_1/acd$) in which the CoO_6 octahedra are compressed along the *c*-axis.[31]

For the time being, magnetic data on polycrystalline $BaCo_3(VO_4)_2(OH)_2$ do not provide definitive evidence for geometrical magnetic frustration within the kagome layers. The value of the ratio of the absolute Weiss temperature to the magnetic ordering temperature, $|\theta|/T_m$, which serves as a frustration index, is moderate, less than 10. The $|\theta|/T_m$ value can however be deceptive in some cases, because the θ value extracted from high-temperature $1/\chi(T)$ data may not reflect the energy scale of a dominant spin-exchange coupling. For example, θ can be a linear combination of different antiferromagnetic and ferromagnetic couplings. Also, we noted that the calculated magnetic susceptibility of isolated (non-interacting) octahedral high-spin Co^{2+} ions has a Curie-Weiss-like behaviour at high temperature with $\theta \approx -20$ K due to the fine structure splitting of the energy levels of the Co^{2+} ion under the action of crystal field, spin-orbit interaction, and magnetic field.[28]

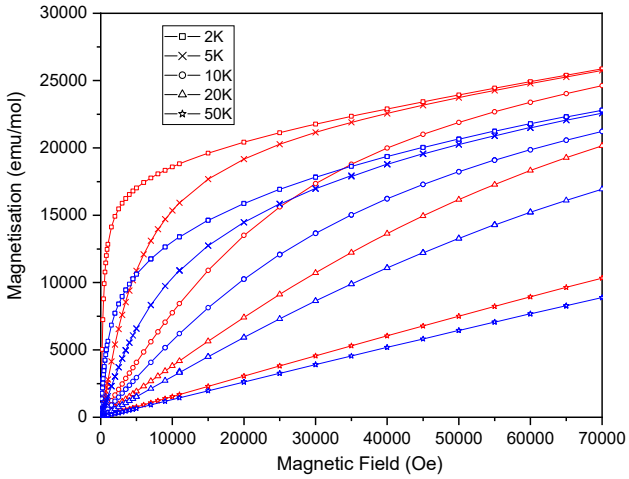

Fig. 8 Magnetic field dependence of magnetisation measured at several temperatures as indicated for **$BaCo_3$-A** (red symbols) and $BaCo_3(VO_4)_2(OH)_2$ nanoparticles[13] (NPs) (blue symbols).

Finally, we turn to the differences between the magnetic behaviour of NPs with a grain size of 20 nm in ref.[13] and those of microstructured samples. These differences occur mainly at low temperatures, T < 10 K. As can be seen in Figs. 6 and 7, χ(T) and χ(T).T increase less rapidly for the NPs with no ZFC-FC magnetic irreversibility down to 2 K. In the absence of any magnetic data for bulk $BaCo_3(VO_4)_2(OH)_2$, such increases and the rapid initial increase of the M(H) curve at 2 K (see Fig. 8) were previously ascribed to finite size or surface effects. Because the susceptibility and isothermal magnetisation behaviours of NPs resemble those of micrometer-sized samples, we can now suggest that highly crystalline NPs with crystallite size of ≈ 20 nm behave as bulk $BaCo_3(VO_4)_2(OH)_2$ with a size-induced decrease of the magnetic ordering temperature. Size-dependent shits of the magnetic ordering temperature have been observed in collinear as well as noncollinear nanostructured antiferromagnets.[32,33]

Conclusions

In this paper, we have presented an alternative synthetic route to produce microstructured $BaCo_3(VO_4)_2(OH)_2$ samples with variable crystallite size in the (*ab*) plane, by using the kagome-

layered pyrovanadate $Co_3V_2O_7(OH)_2{\cdot}2H_2O$ as a starting reagent. This procedure therefore resembles a topochemical reaction as it involves the introduction of Ba^{2+} ions into a pre-shaped $Co_3O_6(OH)_2$ kagome-layered structure. As for NPs, PXRD analyses reveal that the crystal structure of the microstructured $BaCo_3(VO_4)_2(OH)_2$ samples is identical to that previously reported for single-crystals. Our susceptibility and magnetisation data suggest that micrometer-sized samples with crystallite sizes lower or higher than 100 nm possess a weak ferromagnetic order below 3 K. Also, these results shed new light on previously published low-temperature magnetic measurements of highly crystalline NPs with sizes in the range of 9-25 nm. The magnetic properties of these NPs could be explained by a size-induced decrease of the magnetic transition.

Author Contributions

The manuscript was written through contributions of all authors. All authors have read and given approval to the final version of the manuscript.

Conflicts of interest

There are no conflicts to declare.

Acknowledgements

The authors thank Nicolas Stéphant, Stéphane Grolleau, and Jean-Yves Mévellec for assistance with physicochemical and spectroscopic characterizations. B.H. and C.P. thank Didier Dufeu, Eric Eyraud, Stéphane Suire, and Thomas Hauet (Réseau francophone de magnétométrie) for their help with magnetic measurements and for helpful discussions. This work was supported by the CNRS, Nantes Université, the Ministère de l'Enseignement Supérieur et de la Recherche, and the French Agence Nationale de la Recherche under Grant No. ANR-18-CE30-0022-04.

Notes and references

1 Y. Okamoto, H. Yoshida and Z. Hiroi, *J. Phys. Soc. Jpn.*, 2009, **78**, 033701.
2 W. Zhang, H. Ohta, S. Okubo, M. Fujisawa, T. Sakurai, Y. Okamoto, H. Yoshida and Z. Hiroi, *J. Phys. Soc. Jpn.*, 2010, **79**, 023708.
3 R. H. Colman, F. Bert, D. Boldrin, A. D. Hillier, P. Manuel, P. Mendels and A. S. Wills, *Phys. Rev. B*, 2011, **83**, 180416.
4 J. A. Quilliam, F. Bert, R. H. Colman, D. Boldrin, A. S. Wills and P. Mendels, *Phys. Rev. B*, 2011, **84**, 180401.
5 Y. Okamoto, M. Tokunaga, H. Yoshida, A. Matsuo, K. Kindo and Z. Hiroi, *Phys. Rev. B*, 2011, **83**, 180407.
6 M. Yoshida H. ;. Michiue, Y. ;. Takayama-Muromachi, E. ;. Isobe, *J. Mater. Chem.*, 2012, **22**, 18793.
7 M. Yoshida, Y. Okamoto, M. Takigawa and Z. Hiroi, *J. Phys. Soc. Jpn.*, 2013, **82**, 013702.
8 D. Boldrin, K. Knight and A. S. Wills, *J. Mater. Chem. C*, 2016, **4**, 10315–10322.
9 H. Ishikawa, T. Yajima, A. Miyake, M. Tokunaga, A. Matsuo, K. Kindo and Z. Hiroi, *Chem. Mater.*, 2017, **29**, 6719–6725.
10 A. Zorko, F. Bert, A. Ozarowski, J. van Tol, D. Boldrin, A. S. Wills and P. Mendels, *Phys. Rev. B*, 2013, **88**, 144419.
11 D. Boldrin, B. Fåk, E. Canévet, J. Ollivier, H. C. Walker, P. Manuel, D. D. Khalyavin and A. S. Wills, *Phys. Rev. Lett.*, 2018, **121**, 107203.
12 D. E. Freedman, R. Chisnell, T. M. McQueen, Y. S. Lee, C. Payen and D. G. Nocera, *Chem. Commun.*, 2011, **48**, 64–66.
13 R. Dessapt, L. Lajaunie, J. J. Calvino, P. Deniard, I. Trenque and C. Payen, *J. Mater. Chem. C*, 2022, **10**, 3287–3291.
14 Y. Haraguchi, T. Ohnoda, A. Matsuo, K. Kindo and H. A. Katori, *Phys. Rev. B*, 2022, **106**, 214421.
15 C. Broholm, R. J. Cava, S. A. Kivelson, D. G. Nocera, M. R. Norman and T. Senthil, *Science*, 2020, **367**, eaay0668.
16 J. R. Chamorro, T. M. McQueen and T. T. Tran, *Chem. Rev.*, 2021, **121**, 2898–2934.
17 M. Zhesheng, H. Ruilin and Z. Xiaoling, *Acta Geol. Sin. - Engl. Ed.*, 1991, **4**, 145–151.
18 T. Đordević and L. Karanović, *Acta Crystallogr. C*, 2013, **69**, 114–118.
19 A. V. Kasatkin, J. Plasil, I. V. Pekov, D. I. Belakovskiy, F. Nestola, J. Cejka, M. F. Vigasina, F. Zorzi and B. Thorne, *J. Geosci.*, 2015, **60**, 251–257.
20 C. Guillemin, *Bull. Minéralogie*, 1956, **79**, 219–275.
21 S. Zhang, H. Yun and H. Yu, *J. Alloys Compd.*, 2018, **735**, 700–706.
22 V. Petricek, M. Dusek and L. Palatinus, *Z. Für Krist.*, 2014, **229**, 345–352.
23 R. W. Cheary and A. Coelho, *J. Appl. Crystallogr.*, 1992, **25**, 109–121.
24 R. W. Cheary and A. A. Coelho, *J. Appl. Crystallogr.*, 1998, **31**, 851–861.
25 R. W. Cheary and A. A. Coelho, *J. Appl. Crystallogr.*, 1998, **31**, 862–868.
26 S. Ni, T. Li and X. Yang, *Mater. Lett.*, 2011, **65**, 2662–2664.
27 P. Y. Zavalij, F. Zhang and M. S. Whittingham, *Acta Crystallogr. C*, 1997, **53**, 1738–1739.
28 F. E. Mabbs and D. J. Machin, *Magnetism and Transition Metal Complexes*, Chapman and Hall, 1973.
29 F. Lloret, M. Julve, J. Cano, R. Ruiz-García and E. Pardo, *Inorganica Chim. Acta*, 2008, **361**, 3432–3445.
30 J. B. Goodenough, *Phys. Rev.*, 1968, **171**, 466–479.
31 Z. He, D. Fu, T. Kyômen, T. Taniyama and M. Itoh, *Chem. Mater.*, 2005, **17**, 2924–2926.
32 S. Thota, J. H. Shim and M. S. Seehra, *J. Appl. Phys.*, 2013, **114**, 214307.
33 D. Zákutná, A. Alemayehu, J. Vlček, K. Nemkovski, C. P. Grams, D. Nižňanský, D. Honecker and S. Disch, *Phys. Rev. B*, 2019, **100**, 184427.

Electronic Supplementary Information

Microstructured layered-kagome $BaCo_3(VO_4)_2(OH)_2$ with variable crystallite size: alternative synthetic route and comparison with nanostructured samples

Bachchar Hadrane,[a] Philippe Deniard,[a] Cassandre Jeannot,[a] Isabelle Trenque,[a] Rémi Dessapt*[a] and Christophe Payen*[a]

[a] *Nantes Université, CNRS, Institut des Matériaux de Nantes Jean Rouxel, IMN, F-44000 Nantes*

Table of contents:

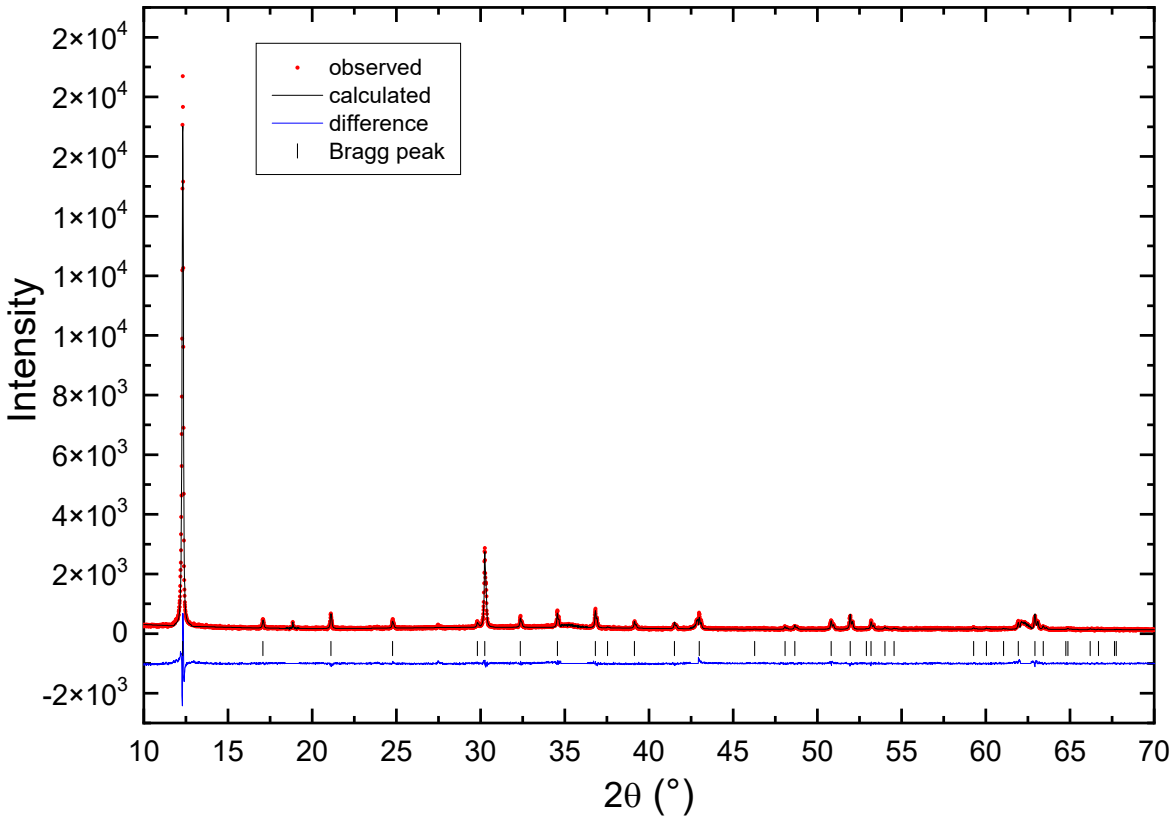

Figure S1. Rietveld refinement plot for $Co_3V_2O_7(OH)_2 \cdot 2H_2O$ showing observed, calculated and difference patterns. The high-level noisy pattern is due to cobalt fluorescence.

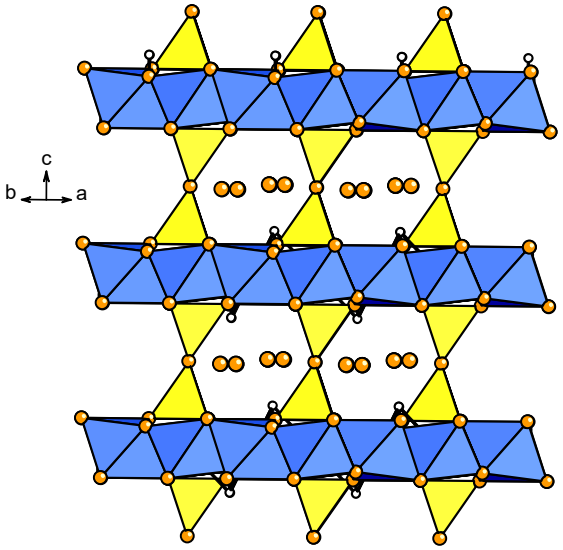

Figure S2. Crystal structure of $Co_3V_2O_7(OH)_2 \cdot 2H_2O$. Blue octahedra: CoO_6, yellow tetrahedra: VO_4, orange sphere: oxygen, white sphere: hydrogen.

Table S1. Structural parameters and crystallite size of $Co_3V_2O_7(OH)_2 \cdot 2H_2O$.

SG $P\bar{3}m$: a=5.9886(3) Å, c=7.1804(4) Å, Cryst. size=217(5) nm ⊥ [001]						
Atom	x	y	z	SOF		U_{iso} Equiv (Å^2)
Co_1	0.5	0	0	1		0.019(7)
V_1	0	0	0.2494(16)	1		0.034(7)
O_1	0.6667	0.3333	0.874(5)	1		0.000(7)
O_2	0.155(3)	0.311 (5)	0.829 (2)	1		0.000
O_3	0	0	0.5	1		0.000
O_4	0.7548(13)	0.374(6)	0.482(12)	1		0.000
H_1	0.6667	0.3333	0.75*	1		0.02*
GOF= 1.41, Rwp= 9.49, Rp= 7.43						

Aniso. ADP (Å^2)	U^{11}	U^{22}	U^{33}	U^{12}	U^{13}	U^{23}
Co_1	0.013(9)	0.002(10)	0.039(6)	0.001(5)	0.014(11)	0.03(2)
V_1	0.032(10)	0.032	0.037(9)	0.0216(5)	0	0

*not refined

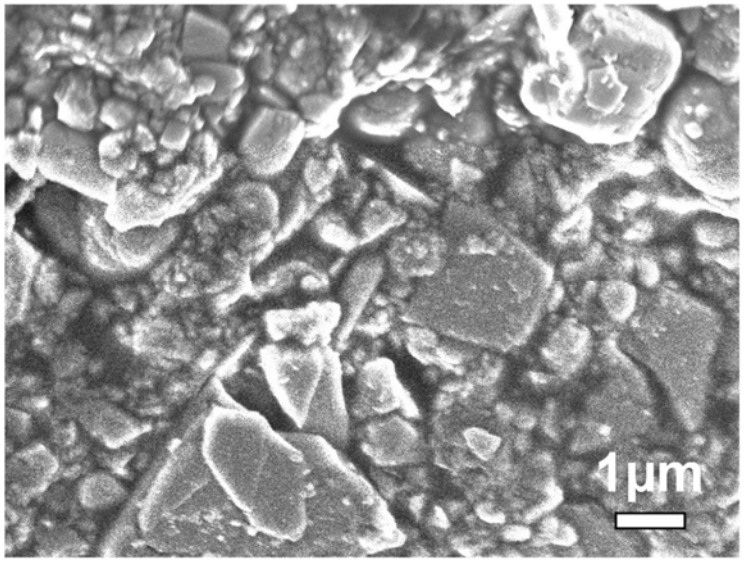

Figure S3. SEM image of $Co_3V_2O_7(OH)_2 \cdot 2H_2O$.

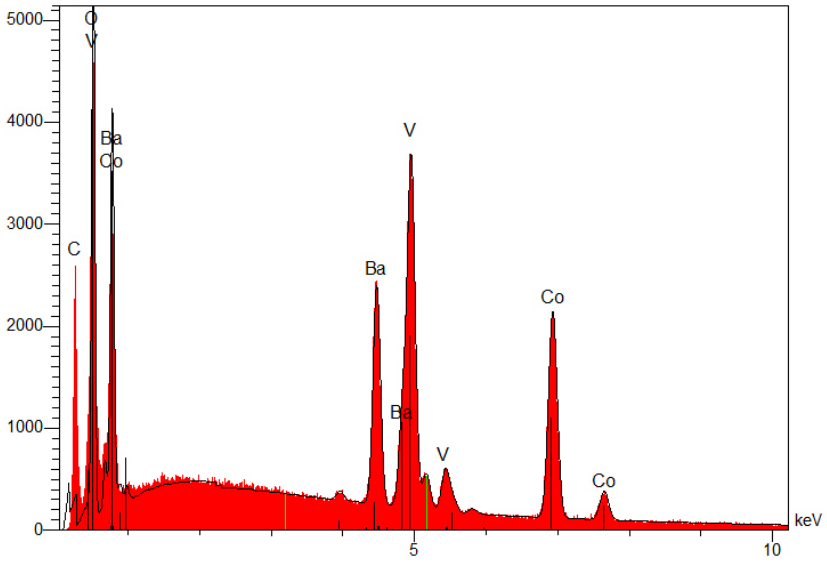

Figure S4. EDS spectrum acquired on micrometric particles of **$BaCo_3$-A** (a similar spectrum has been obtained for **$BaCo_3$-B**).

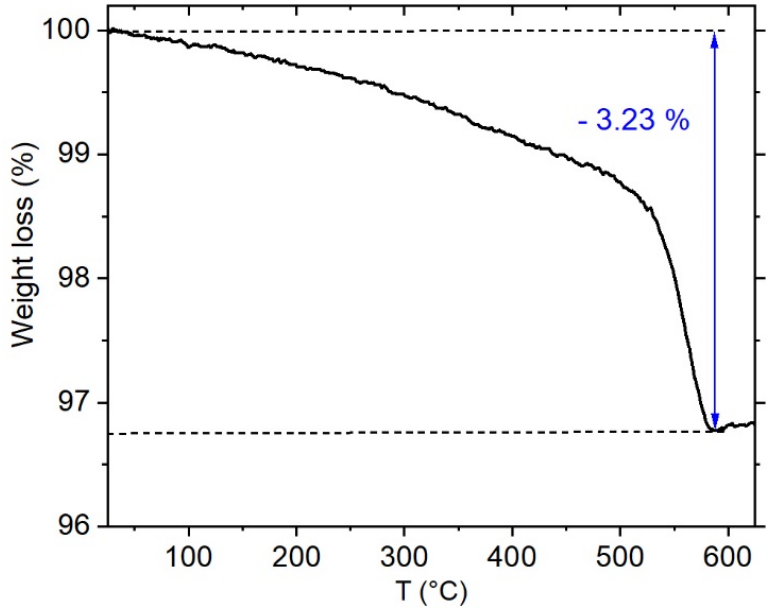

Figure S5. Thermogravimetric curve of microstructured **$BaCo_3$-B** recorded in air.

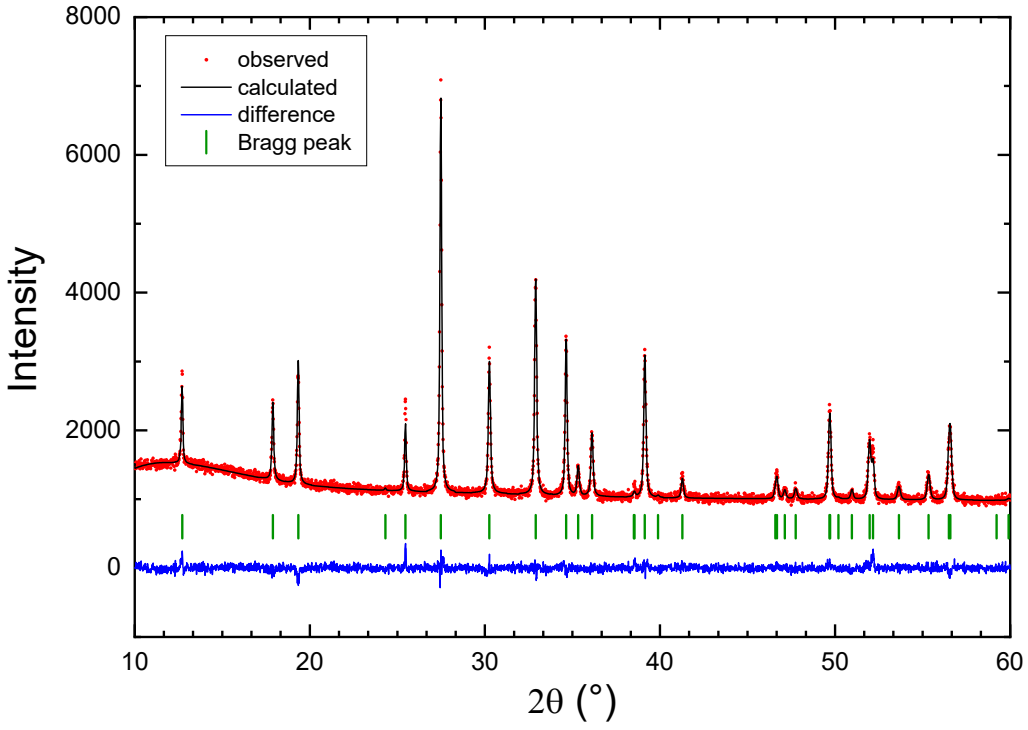

Figure S6. Rietveld refinement plot for microstructured **$BaCo_3$-B** showing observed, calculated and difference patterns. The high-level noisy pattern is due to cobalt fluorescence.

Table S2. Structural parameters and crystallite size of **$BaCo_3$-B**.

SG $R\bar{3}m$: a=5.9238(2) Å, c=21.0609(9) Å, Cryst. size=92(3) nm ⊥ [001], 47(5) nm // [001]						
Atom	x	y	z	SOF		U_{iso} Equiv (Å^2)
Ba_1	0.6667	0.3333	0.8333	1		0.033(2)
Co_1	0.8333	0.6667	0.6667	1		0.013 (2)
V_1	0.3333	0.6667	0.7527(3)	1		0.015(3)
O_1	0.3333	0.6667	0.832(8)	1		0.005 (3)
O_2	0.4930(9)	0.5070(10)	0.7275(4)	1		0.005
O_3	0	0	0.7030(10)	1		0.005
H_1	0	0	0.7494*	1		0.008*
GOF= 1.11, Rwp= 3.32, Rp= 2.62						

*not refined

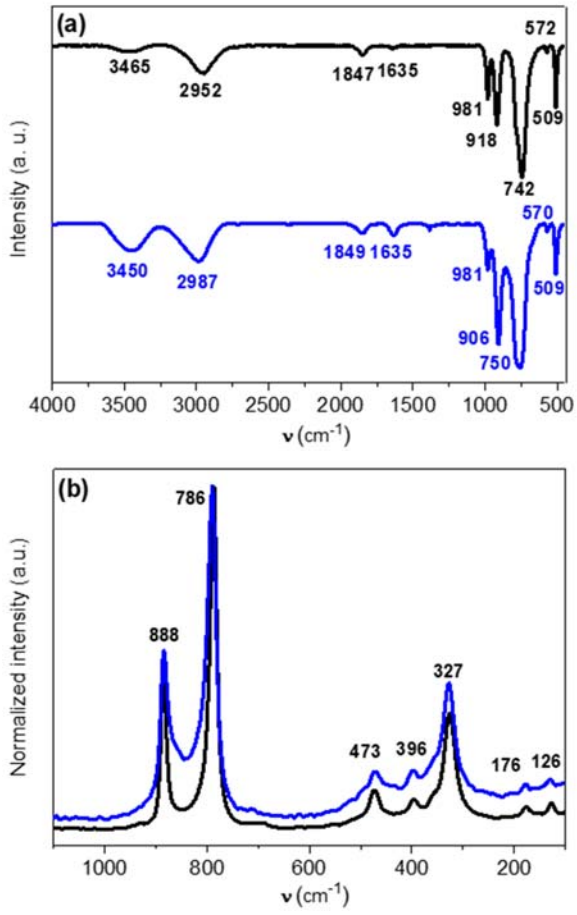

Figure S7. Comparison of (a) FT-IR and (b) Raman spectra of microstructured **$BaCo_3$-B** (black line) and $BaCo_3(VO_4)_2(OH)_2$ nanoparticles[S1] (NPs) (blue line).

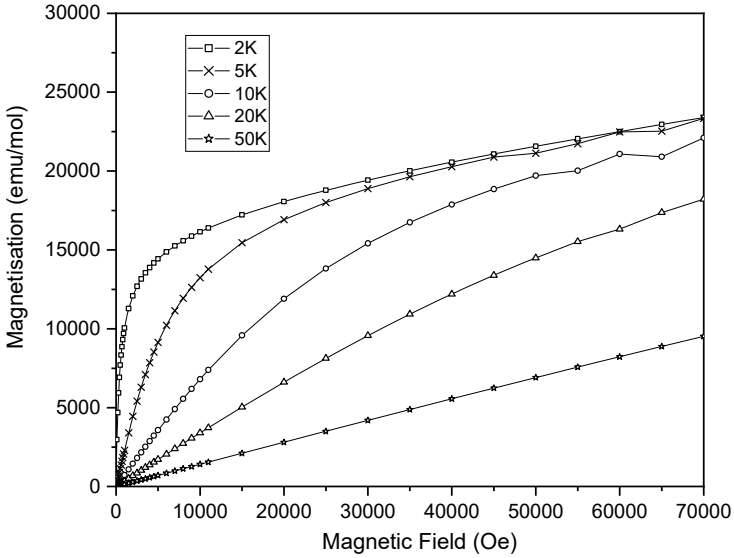

Figure S8. Magnetic field dependence of magnetisation measured at several temperatures for **$BaCo_3$-B**.

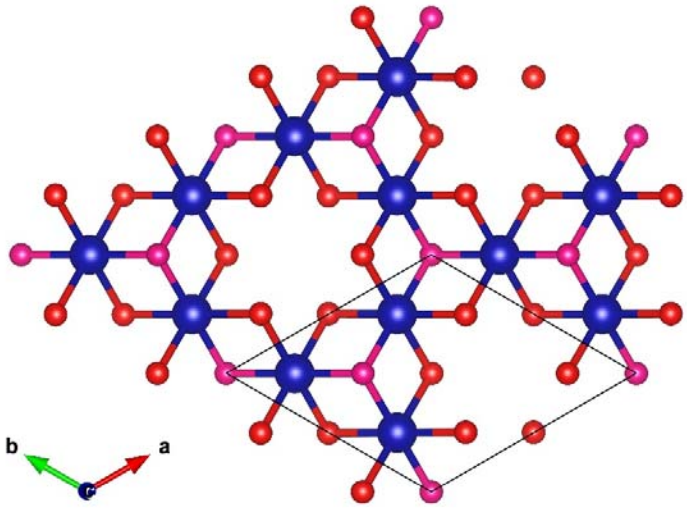

Figure S9. Fragment of a kagome layer in the $BaCo_3(VO_4)_2(OH)_2$ crystal structure (projection along [001] direction). Blue, red, and pink spheres represent Co, O2, and O3 atoms (see Tables 1 and S2), respectively. Barium, vanadium, and hydrogen atoms have been removed for clarity. Each kagome layer is formed from compressed $Co(O2)_4(O3)_2$ octahedra with dCo-O2 = 2.176(4) Å and dCo-O3 = 1.9407(6) Å.

References

[S1] R. Dessapt, L. Lajaunie, J. J. Calvino, P. Deniard, I. Trenque and C. Payen, *J. Mater. Chem. C*, 2022, **10**, 3287-3291.